Master Thesis

Escola Tècnica Superior
d'Enginyeria Industrial de Barcelona

Modeling and Analysis of an Islanded, Low Voltage, Inverter-Based Microgrid

Author: **Christian Ribback**

Director: **Eduard Bullich-Massagué, PhD**

Co-Director: **Mònica Aragüés-Peñalba, PhD**

Barcelona, September 2019

Acknowledgment

I would like to express my gratitude to Eduard Bullich-Massagué and Mònica Aragüés-Peñalba for supervising my thesis. I really appreciated the freedom I was given in setting the objectives and scheduling my working hours during the last semester. The discussions we had gave me clear directions on where the thesis was headed and I always left our meetings feeling a strong motivation to keep going.

César Valderrama, thank you for being such a great program coordinator. You too made this last year in Barcelona unforgettable.

My thesis would have looked very differently if I had not taken Eduardo Prieto-Araujo's class on converter control. Thank you for a great introduction to this topic in the Fall semester 2018.

Ben and Astrid, I hope we will see each other again soon and maybe share a flat in another city!

Abstract

The penetration of Voltage Source Converters (VSCs) interfacing renewable energy sources in today's power system has experienced a steep incline. In microgrids, the penetration of VSCs can reach 100% during times when the load is supplied exclusively through renewables in combination with battery storage, providing a research field regarding VSC interaction and control.

In this thesis, a real low-voltage, islanded microgrid in Thailand is modelled in *Simulink* with the *Simscape Power Systems* library. The system consists of a 40 kW PV array, 240 kWh lead-acid battery and a 50 kW diesel generator with a peak load of 25 kW at a lagging power factor of 0.95. The diesel generator has been omitted to simulate an inverter-based microgrid and focus on VSC interaction.

The battery-interfacing VSC is controlled as a grid-forming converter, whereas the PV-interfacing VSC is operated in grid-feeding mode. Both VSCs are controlled in the *(qd)*-frame. During peak-load condition the simulation shows a minimum voltage of 0.89 pu at the load bus. Therefore, a third, small-scale battery-interfaced VSC in closer proximity to the load is integrated and operated in grid-supporting mode with the objective to maintain a minimum load bus voltage of 0.95 pu.

It is shown that a 21 kVA-rated VSC can provide adequate voltage regulation through active power injection if operated in current-control mode with Pv-droop control, given the resistive nature of the low voltage lines. Reactive power can be shared among the VSCs through frequency adjustments of the grid-forming converter. The droop control of the grid-supporting VSC is extended with a dead band to regulate its participation to voltage control. The simulations show that the microgrid remains stable during large load steps, if the droop constants of the forming converter are below $\approx 4\%$.

Contents

List of Figures

List of Tables

Chapter 1

Introduction

1.1 Context

The electricity sector is undergoing an unprecedented transition away from centralized, large-scale power generation, to small-scale and decentralized generation units, referred to as *Distributed Energy Resources (DER)*. This transition poses significant technical challenges with regards to grid management and control, as the majority of DER are intermittent in nature and uncertain, with little degree of controllability [4].

Microgrids can provide a pathway to integrating larger shares of renewables to the power system [17]. This can be achieved by dealing with control complexity in a decentralized manner and on a smaller scale. This means that no large, central coordination unit is required. A microgrid can therefore act a controllable unit to the hosting grid to which it is connected through a single *Point of Common Coupling (PCC)*. Within the microgrid, voltage and frequency control can become complex if the majority of power is delivered through power-electronic interfaced units, due to a lack of *system inertia* [3]. If a microgrid is not connected to a hosting grid it is continuously operated in *islanded*-mode. In this case, power balance and voltage control is exclusively maintained through coordination of each participating DER, rendering it the most complex control case [3, 15].

Demonstrated technical and economical feasibility of renewable energy and storage technologies have led to a higher share of inverter-connected generating units, which necessitates advanced control schemes to ensure reliable supply of electricity [3]. DERs and *Energy Storage Systems (ESS)* are typically interfaced to the AC-grid through *Voltage Source Converters (VSCs)*, making VSC-control an integral part of this thesis.

The small-scale, low voltage, AC-microgrid on the Thai island *Koh Jik* feeds its load primarily through centralized solar PV (40 kW) and a lead-acid based battery system (50 kW, 240 kWh). During daytime operation it can therefore be defined as an *inverter-based* microgrid, as the diesel generator is only turned on in the evening and early morning hours. The 400 inhabitants of Koh Jik draw a peak load of about 25 kW. In this thesis a control scheme for voltage stabilization through a decentralized storage unit is proposed.

1.2 Objectives and Scope

This thesis investigates the dynamic behavior of a low voltage, islanded, inverter-based microgrid operated under a hierarchical control scheme. The operation of the system assumes three-phase balanced and symmetrical conditions.

The research objectives are:

1. Build a detailed *Simulink* model with the *Simscape Power System* library representing the current day-time operation of the Koh Jik microgrid.
2. Size and integrate a grid-supporting converter into the *Simulink* model, which is located in closer proximity to the load center.
3. Implement and discuss a control architecture allowing voltage support by the grid-supporting converter to maintain a minimum voltage of 0.95 pu at the load bus.

Chapter 2

Background

2.1 Microgrid Definitions

A microgrid can be regarded as a autonomous grid incorporating DERs, storage assets and a cluster of loads that is connected to the main grid at a single PCC [3]. DERs, such as *Photovoltaic (PV)*, are interfaced to the grid through VSCs that are typically based on Insulated-Gate Bipolar Transistors (IGBT).

Microgrids can be associated with *Active Distribution Networks*, since power flow within the network is *bi-directional* due to the integration of DERs [4]. Microgrids are suitable solutions to electrify remote areas, which are not connected to the main grid for technical or economical reasons.

2.2 Microgrid Control

The goal of microgrid control is to establish a reliable supply of electricity in the network. Coordination of all connected DERs in a microgrid can be achieved either in a *centralized* or *decentralized* manner. The former requires extensive communication channels, such that each DER can report its operating states to a central server, which passes the appropriate control actions back. In larger networks, this can become unfeasible due to the significant communication and processing power requirements [3].

A fully *decentralized* control relies on each individual DER's local control loops. As the local controllers only receive measurements from their PCCs, system-wide parameters remain unknown. In networks with various DER units this approach can become unfeasible due to the potential strong coupling between the operation of each unit [3].

A middle ground of both approaches is based on a three-level hierarchical control system, in which each level differs with regards to speed and equipment requirement. The response time difference decouples the control dynamics of the layers, which allows a separate design [6]. The control layers are split into: *Primary*, *Secondary* and *Tertiary* control [3]. Figure 2.1 depicts the different control layers.

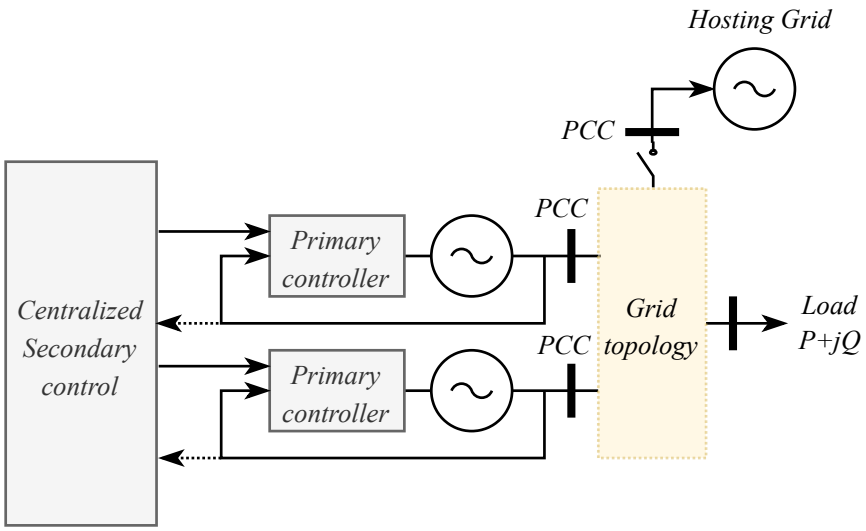

Figure 2.1: Primary and centralized Secondary Control interaction in islanded microgrid

2.2.1 Primary Control

Primary control builds the *lowest* level of the hierarchical control layout. It usually relies only on local measurements of the VSC's output voltage and current and operates in the fastest time regime [3].

Therefore, it is crucial to restore local *transient* disturbances, for example caused by a load step. The primary control layer can be split into an *inner*- and *outer*-control loop, which will be elaborated in Section 2.5.

2.2.2 Secondary Control

Secondary control is tasked with correcting steady-state frequency and voltage deviation, which can be caused by deploying the *droop*-control concept in the outer loop of the primary control block [6]. Secondary control can be coordinated through a *centralized* microgrid control unit, which processes measurements from individual VSCs and computes separate restoration terms for each unit.

Distributed secondary control can be based on a common communication link between each VSC, allowing to exchange measurement data between the local controllers and taking corresponding control actions.

Secondary control can also be deployed without the use of communication links. This way, frequency and voltage restoration are achieved only locally, which can cause stability issues [6].

2.2.3 Tertiary Control

Tertiary control is employed during grid-connected mode, to establish setpoints at the PCC of microgrid and hosting grid. As this thesis deals with an islanded microgrid, this control layout will not be further analyzed.

2.3 Review of AC Power Flow

This section provides a brief introduction in the equations governing active and reactive power flow in AC systems. Figure 2.2 represents a VSC as a controlled voltage source with output voltage $\underline{v}_z$ connected via an impedance $\underline{Z}$ to a common AC bus with voltage $\underline{v}_g$.

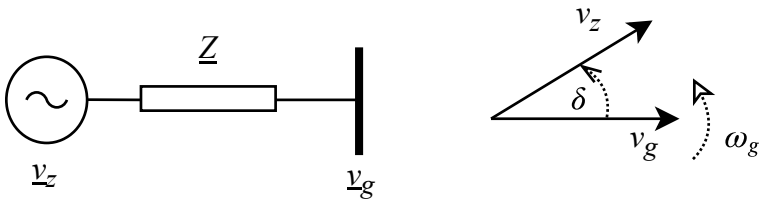

Figure 2.2: Converter and grid voltage phasor representation

In high-voltage networks, the impedance $\underline{Z}$ is mainly inductive simplifying the power flow equations to [12]:

$$P \approx \frac{v_z v_g}{X} sin(\delta), \qquad Q \approx \frac{v_z^2 - v_z v_g}{X} cos(\delta) \tag{2.1}$$

In 2.1, v_g and v_z stand for the magnitude of the grid and converter output voltage phasors, respectively. The phase displacement between both voltage phasors is represented by δ. For small displacements, (2.1) can be linearized as $sin(\delta) \approx \delta$ and $cos(\delta) \approx 1$. Thus:

$$P \approx \frac{v_z v_g}{X} \delta, \qquad Q \approx \frac{v_z^2 - v_z v_g}{X} \tag{2.2}$$

It can be seen that the active power can be controlled by the phase displacement δ, whereas reactive power is controlled through a voltage magnitude difference. The phase displacement is dynamically controlled through the angular frequency ω. Turning this around, controlling the active and reactive power output of the converter allows to regulate the frequency and voltage at the PCC.

For low-voltage networks, however, $\underline{Z}$ is largely resistive. Thus, the reactance can be neglected, leading to the following power flow equations:

$$P \approx \frac{v_z^2 - v_z v_g}{R}, \qquad Q \approx -\frac{v_z v_g}{R} \delta \tag{2.3}$$

Thus, for low-voltage networks, controlling active power regulates the voltage, whereas reactive power regulates the frequency at the PCC [12].

2.4 Converter Model

The dynamics between a converter and an AC system can be captured by a *switched* or an *averaged* converter model. The former contains the instantaneous values of voltage and current that are present due to the discrete switching states of the converter, thus containing high-frequency components. While this representation models the dynamics closest to reality, it is difficult to derive a control logic for the main control signal, the modulation index. In addition, converters are connected through filter components to AC networks, which have low-pass characteristics, thus attenuating high-frequency signals [16].

The averaged model analyzes the dynamics of the averaged variables, instead of the instantaneous ones of the switched model. The converter terminal voltage v_c is averaged over the period of the carrier signal, T_s [16]:

$$v_c(t) = \frac{1}{T_s}\int_0^{T_s} v_c(\tau)d\tau + \sum_{h=0}^{h=\infty}[a_h cos(h\omega_s t) + b_h sin(h\omega_s t)] \tag{2.4}$$

Where h is the harmonic order and ω_s is the angular frequency of the carrier signal. Further:

$$a_h = \frac{2}{T_s}\int_0^{T_s} v_c(\tau)cos(h\omega_s\tau)d\tau, \qquad b_h = \frac{2}{T_s}\int_0^{T_s} v_c(\tau)sin(h\omega_s\tau)d\tau \tag{2.5}$$

Since the filter interface (L_f) exhibits low-pass behavior, the high-frequency components of $v_c(t)$ will have a negligible effect on the output current i_c, thus assuming no ripple current. Note that here $v_c(t)$ represents the average terminal voltage of the converter and should not be confused with $v_z(t)$ from Section 2.3, which represents the voltage *after* the filter.

2.5 VSC Control Structure

This section provides a detailed explanation of the cascaded loops of the inner control level that regulate the output current and voltage of the VSC.

The general scheme of a VSC is shown in Figure 2.3 [14]. Simplified, a VSC consists of a DC-bus connected to a DC/AC converter. In this thesis, a 2-level converter topology is used working with IGBTs. Assuming an ideal DC-source, the dynamics of the DC-bus are neglected. The converter is connected to the grid through an *RLC*-filter. The inductance attenuates high-frequency current ripples caused by the IGBT switchings in the *kilo-hertz (kHz)* range. The shunt capacitor attenuates voltage deviations and allows to control the output voltage of the converter. The subscript c stands for converter terminal values, z denotes the PCC-values and g describes the states of the grid.

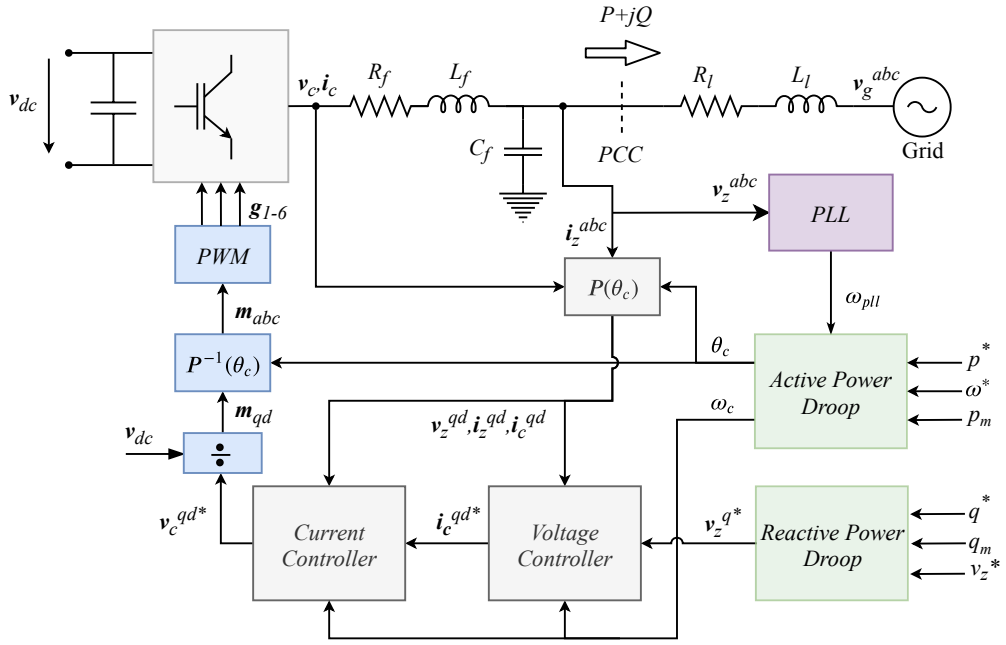

Figure 2.3: VSC control structure

The control structure can be split into *inner*- cascaded control loops (*grey*), the *outer*-control loops (*green*), a *Phase-Locked Loop (PLL)* (*purple*), and a modulation process including the *Pulse-Width Modulation*-block (*blue*). To simplify the control of sinusoidal quantities, voltage and current signals are transformed into the *(qd)*-frame. This allows to represent three-phase sinusoidal quantities as DC-values for balanced grid conditions, hence enabling the use of PI-controllers.

The *PLL* is required to derive the angular frequency ω at the PCC. A *Power Measurement*-block, computing the instantaneous p_m and q_m, has been omitted in Figure 2.3. The *outer* loop is based on *droop-control* and generates the reference voltage signal (magnitude v_z^{q*} and angular frequency ω_c), which is passed to the inner control loop, consisting of a cascaded voltage and current loop. In the modulation process, the converter voltage setpoint (v_c^{qd*}), is transformed into the modulation

index m_{qd} and subsequently converted back to the *(abc)*-frame. The *PWM*-block generates the switching sequence for the 6 individual IGBTs (g_{1-6}).

2.5.1 State Equations

The equations governing the AC-side dynamics of the filter are critical to understand the VSC control structure. The voltage drop across the *RL*-element, described *(qd)*-frame is given by:

$$v_z^q - v_c^q = R_f i_q + L_f \omega i_d + L_f \frac{di_q}{dt} \tag{2.6}$$

$$v_z^d - v_c^d = R_f i_d - L_f \omega i_q + L_f \frac{di_d}{dt} \tag{2.7}$$

The current flowing into the filter capacitor C_f is described by:

$$i_c^q - i_z^q = \omega C_f v_z^d + C_f \frac{dv_z^q}{dt} \tag{2.8}$$

$$i_c^d - i_z^d = -\omega C_f v_z^d + C_f \frac{dv_z^d}{dt} \tag{2.9}$$

The equations reveal coupling between *(qd)*-components. The controller design needs to compensate the coupling, which is described in the following section.

2.5.2 Inner Control Loops

The inner control consists of a cascaded voltage- and a current loop. Neglecting the delay effect imposed by the PWM, the interaction of state variables can be presented in the Laplace domain by their respective transfer functions (see Figure 2.4).

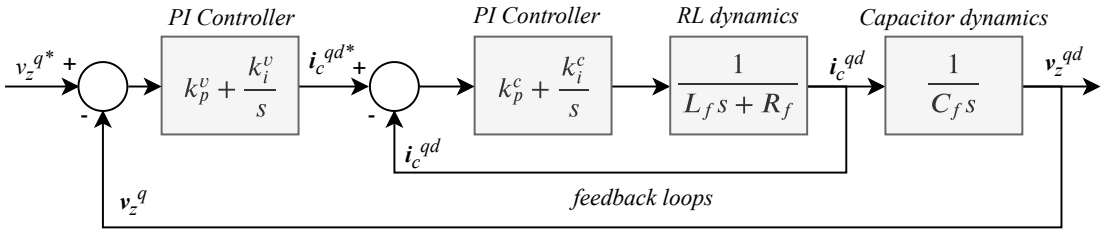

Figure 2.4: Cascaded voltage- and current loop

In the following each loop is elaborated in more detail.

Current Control Loop

The objective of the current loop is to regulate the converter current through the filter inductance, such that $i_c^{qd} = i_c^{qd*}$. This is achieved through a closed loop architecture and performed for the *(qd)*-components separately.

For simplicity, the following explanation focuses on the *(q)*-component exclusively: The difference between measured (i_c^q) and reference (i_c^{q*}) is passed to a PI-controller, whose output is $\hat{v}_c^q$. A decoupling feed-forward achieves that $\hat{v}_c^q$ is not dependent on *(d)*-components anymore. Recall that the coupling is present due to the AC-dynamics of the *RL*-element (see (2.6)). Assuming that the delay effect of the PWM process is negligible, the open-loop transfer function of the current controller would be of the form:

$$\frac{i_c^q}{i_c^{q*}} = K(s)\frac{1}{L_f s + R_f} \tag{2.10}$$

Where $K(s)$ denotes the transfer function of the PI compensator. The decoupling feed-forward allows the PI-controllers to only regulate the decoupled-terms of (2.6) (2.7), which are:

$$\hat{v}_c^q = -R_f i_q + L\frac{di_q}{dt}, \qquad \hat{v}_c^d = -R_f i_d + L\frac{di_d}{dt} \tag{2.11}$$

Subsequently, the decoupled term is added (fed-forward). Rearranging (2.6, 2.7) for v_c^{qd*} and converting it to Laplace domain gives:

$$v_c^{q*} = v_z^q - \left(k_p^c + \frac{k_i^c}{s}\right)(i_c^{q*} - i_c^q) - L_f\omega_c i_c^d \tag{2.12}$$

$$v_c^{d*} = v_z^d - \left(k_p^c + \frac{k_i^c}{s}\right)(i_c^{d*} - i_c^d) + L_f i_c^q \tag{2.13}$$

Thus, from a control flow perspective, the output of the current loop is the converter output voltage, which is sent to the PWM block. The equations are represented in a control diagram in Figure 2.5. Note that the *Modulation* section has been included in this diagram to understand how the current control loop fits into the overall VSC control scheme. Interested readers can find more elaborate explanations of the current loop in [16].

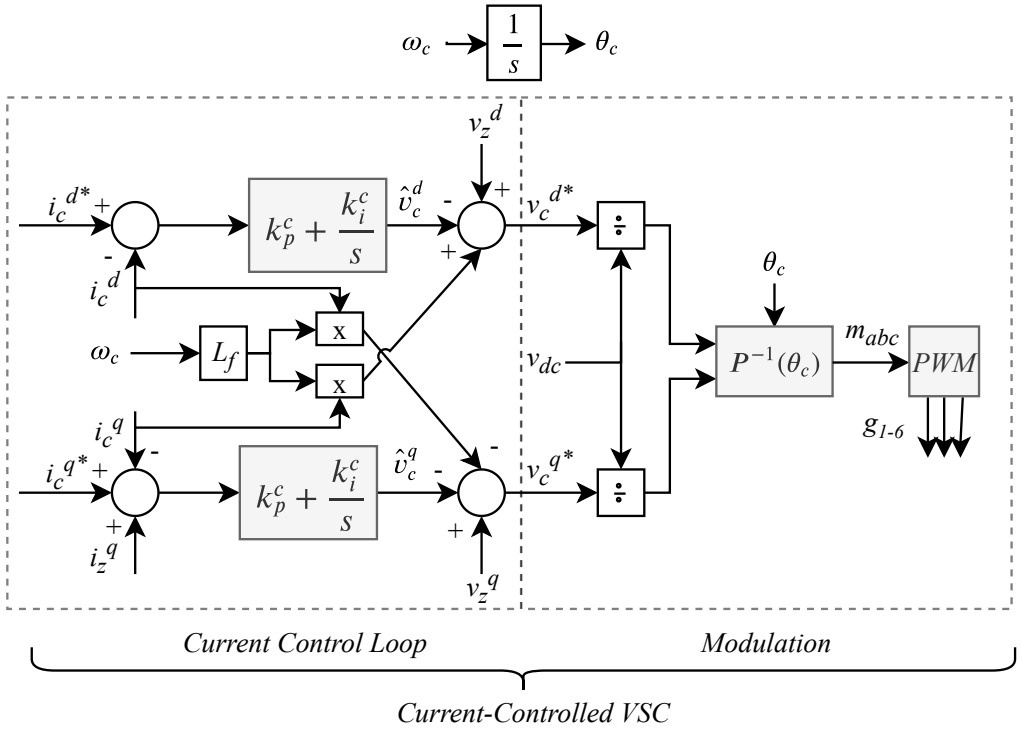

Figure 2.5: Current-Controlled VSC schematic

Voltage Control Loop

The objective of the voltage loop is to regulate the voltage at the capacitor (v_z^{qd}) to a desired reference value (v_z^{qd*}) through a closed loop approach. Recall that the capacitor dynamics, described in (2.8, 2.9), introduce coupling between *(qd)*-components. To decouple the state equations for the capacitor, a similar approach is taken as in the current loop.

$$\hat{i}_c^q = C_f \frac{dv_c^q}{dt}, \qquad \hat{i}_c^d = C_f \frac{dv_c^d}{dt} \tag{2.14}$$

By adding the coupled terms to the equation for the reference current signal yields in Laplace domain:

$$i_c^{q*} = i_z^q + \left(k_p^v + \frac{k_i^v}{s}\right)(v_z^{q*} - v_z^q) + \omega_c C_f v_z^d \tag{2.15}$$

$$i_c^{d*} = i_z^d + \left(k_p^v + \frac{k_i^v}{s}\right)(v_z^{d*} - v_z^d) - \omega_c C_f v_z^q \tag{2.16}$$

The equations are represented in a control diagram in Figure 2.6.

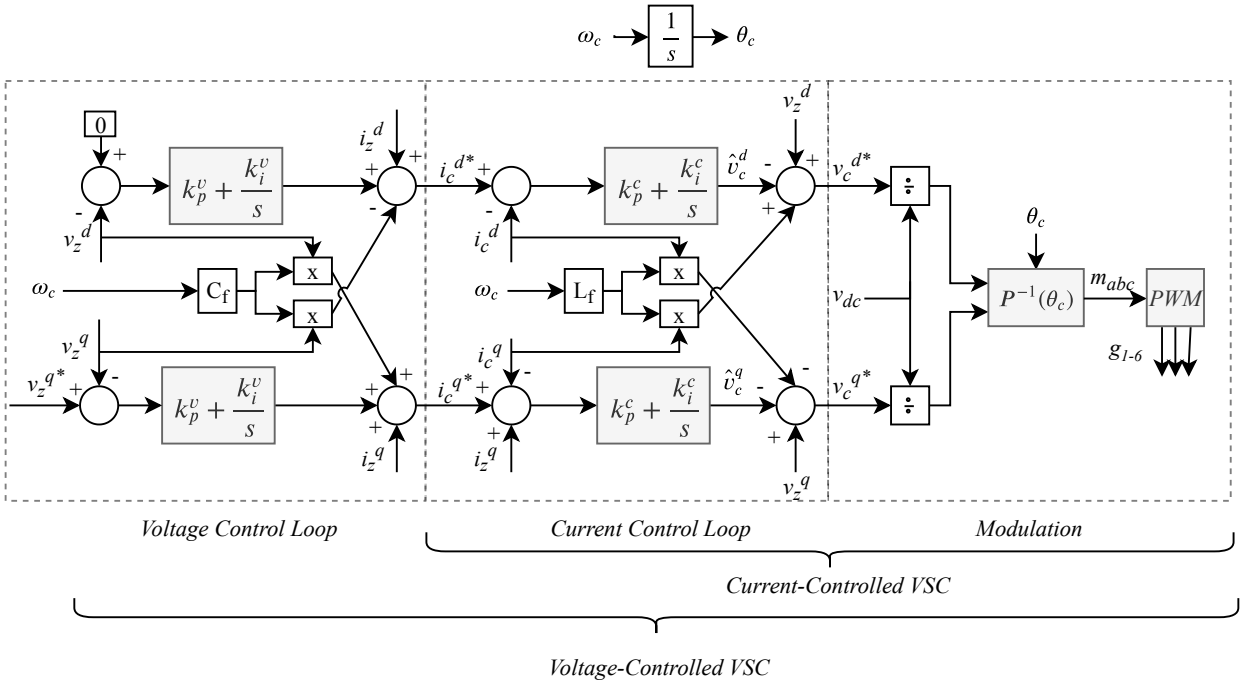

Figure 2.6: Voltage-Controlled VSC schematic

Pulse-Width Modulation

The converter reference voltage signal v_c^{qd*} is used to generate the modulation sequence (m_{abc}) for the VSC. This is achieved through a division with the DC-voltage and an anti-transformation with the angle of the synchronous frame θ, to move from *(qd)*-frame to *(abc)*-frame.

$$m_{abc} = P^{-1}(\theta)\frac{v_c^{qd*}}{v_{dc}} \tag{2.17}$$

$$P^{-1}(\theta) = \begin{bmatrix} cos(\theta) & sin(\theta) & 1 \\ cos(\theta - \frac{2\pi}{3}) & sin(\theta - \frac{2\pi}{3}) & 1 \\ cos(\theta + \frac{2\pi}{3}) & sin(\theta - \frac{2\pi}{3}) & 1 \end{bmatrix} \tag{2.18}$$

Further information on the transformation from *(abc)* to *(qd)*-frame can be found in [7].

2.5.3 Phase-Locked Loop

The PLL is tasked with computing the angular frequency at the point of coupling. Conceptually, the correct frequency is obtained when the *(qd)*-frame rotates at the same frequency as the grid. In this state, the *d*-component of the space vector is zero. In this thesis, a PI-type 2nd order PLL in SRF is used, as proposed in [13].

Its transfer function is:

$$\frac{\hat{\theta}(s)}{\theta(s)} = \frac{2\zeta\omega_n s + \omega_n^2}{s^2 + 2\zeta\omega_n + \omega_n^2} \tag{2.19}$$

Where $\hat{\theta}(s)$ stands for the estimated grid angle while $\theta(s)$ denotes the real grid angle. ζ refers to the damping coefficient, while ω_n stands for the natural frequency of the system.

The tuning of the of k_p^{pll} and k_i^{pll} was carried out according to [13]:

$$\omega_n = \sqrt{\frac{k_p^{pll} E_m}{\tau}} \tag{2.20}$$

$$\zeta = \frac{k_p^{pll} E_m}{2\omega_n} = \frac{\sqrt{k_p^{pll} E_m \tau}}{2} \tag{2.21}$$

Where E_m refers to the peak *line-neutral* voltage. ζ was set to 0.707.

2.5.4 Primary Control based on Droop

The objective of primary control is to stabilize frequency and voltage in a network. Primary control based on droop achieves this through local measurements only. This makes it a very reliable control strategy and offers plug-and-play features.

The droop approach is based on the approximately linear relationship between active power and frequency (Pf) and reactive power and voltage (QV). These equations translate into a proportional controller, with which frequency and voltage amplitude at the PCC can be regulated via the injected p and p, respectively (or vice-versa). The output of the droop regulator for a VSC in voltage-controlled mode are the internal converter frequency and voltage amplitude setpoints [9]. On the other hand, a droop regulator computes p^* and q^* setpoints for a grid-following converter operated in current-controlled mode.

Additionally, a distinction between *static* and *oscillatory* droop is introduced in this work. In *static* droop, ω^* and v_z^* are constant values (i.e. nominal frequency and nominal line-neutral peak voltage). In *oscillatory* droop, ω^* and v_z^* are measured variables and can be provided through a PLL [14].

For a VSC operated in voltage-controlled mode, the general droop equations are:

$$\omega_c = \omega^* - d_p(p^* - \lambda(s)p) \qquad \omega^* = \{\omega_{ref}, \omega_{pll}\} \tag{2.22}$$

$$v_z^{q*} = v_z^* - d_q(q^* - \lambda(s)q) \qquad v_z^* = \{v_{z,ref}^q, v_{z,pll}^q\} \tag{2.23}$$

Where ω_c and v_z^{q*} denote the computed angular frequency and voltage magnitude. $\lambda(s)$ denotes the transfer function of a first order low-pass-filter (LPF), while p and q stand for the measured active and reactive power. The measured power values need to be filtered to stabilize the controller and rejecting disturbances and oscillations [5]. The superscript (*) denotes the respective setpoints.

Figure 2.7 shows the graphic representation of (2.22, 2.23) for a voltage-controlled converter with *static* droop behavior.

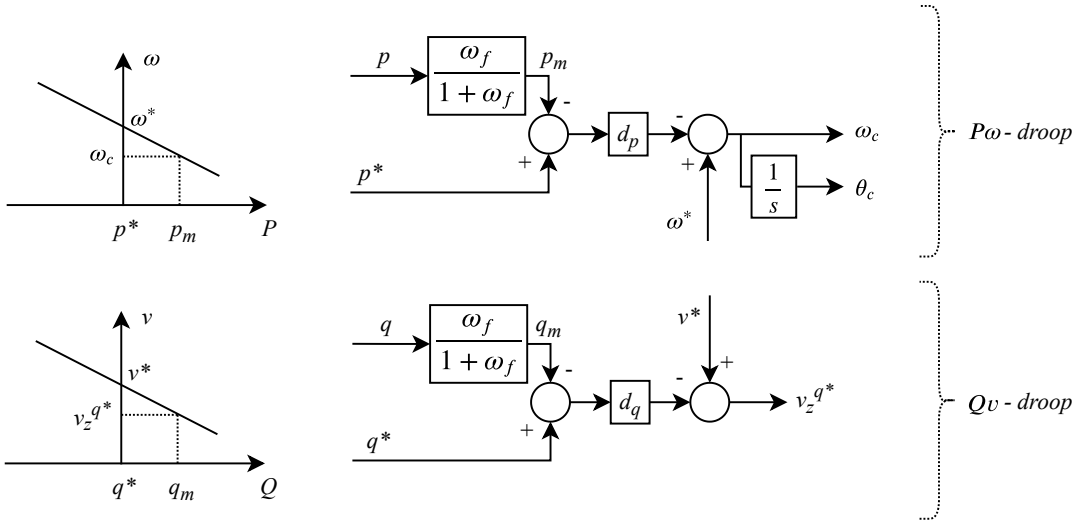

Figure 2.7: $P\omega$ and Qv droop relation

2.5.5 Active and Reactive Power Controller

The objective of the power controller is to achieve a pre-defined active and reactive power output of the converter. This can be achieved by converting a power setpoint (p^*, q^*) into a current setpoint (i_c^{q*}, i_c^{d*}), which is directly passed to the current controller. The active and reactive power delivered to the AC system across the PCC is governed by [16]:

$$p(t) = \frac{3}{2}[v_z^q(t)i_q(t) + v_z^d(t)i_d(t)] \tag{2.24}$$

$$q(t) = \frac{3}{2}[v_z^q(t)i_d(t) - v_z^d(t)i_q(t)] \tag{2.25}$$

In steady-state condition the PLL is synchronized and thus, $v_z^d = 0$, which simplifies (2.24) and (2.25) to:

$$p(t) = \frac{3}{2}[v_z^q(t)i_q(t)] \tag{2.26}$$

$$q(t) = \frac{3}{2}[v_z^q(t)i_d(t)] \tag{2.27}$$

Thus, active and reactive power can be controlled through the *(qd)*-components of the current. Consequently it follows that if the current controller achieves $(i_q = i_q^*)$ and $(i_d = i_d^*)$, it must also hold that $p = p^*$ and $q = q^*$. The current references are computed with:

$$i_c^{q*} = \frac{2}{3}\frac{p^*}{v_z^q} \tag{2.28}$$

$$i_c^{d*} = \frac{2}{3}\frac{q^*}{v_z^q} \tag{2.29}$$

2.5.6 Secondary Control

Droop control leads to steady-state frequency and voltage deviations in the system. As part of secondary control, frequency and voltage restoration loops are employed to drive the steady-state error to zero. The restoration loops compute a $\delta\omega$ and δv that is added to the droop loop output:

$$\delta\omega = k_p^{\omega}(\omega^* - \omega_c) + k_i^{\omega}\int(\omega^* - \omega_c)dt \tag{2.30}$$

$$\delta v = k_p^{u}(v^* - v_z^q) + k_i^{u}\int(v^* - v_z^q)dt \tag{2.31}$$

Figure 2.8 shows how to interpret $\delta\omega$ and δv in the context of the droop control.

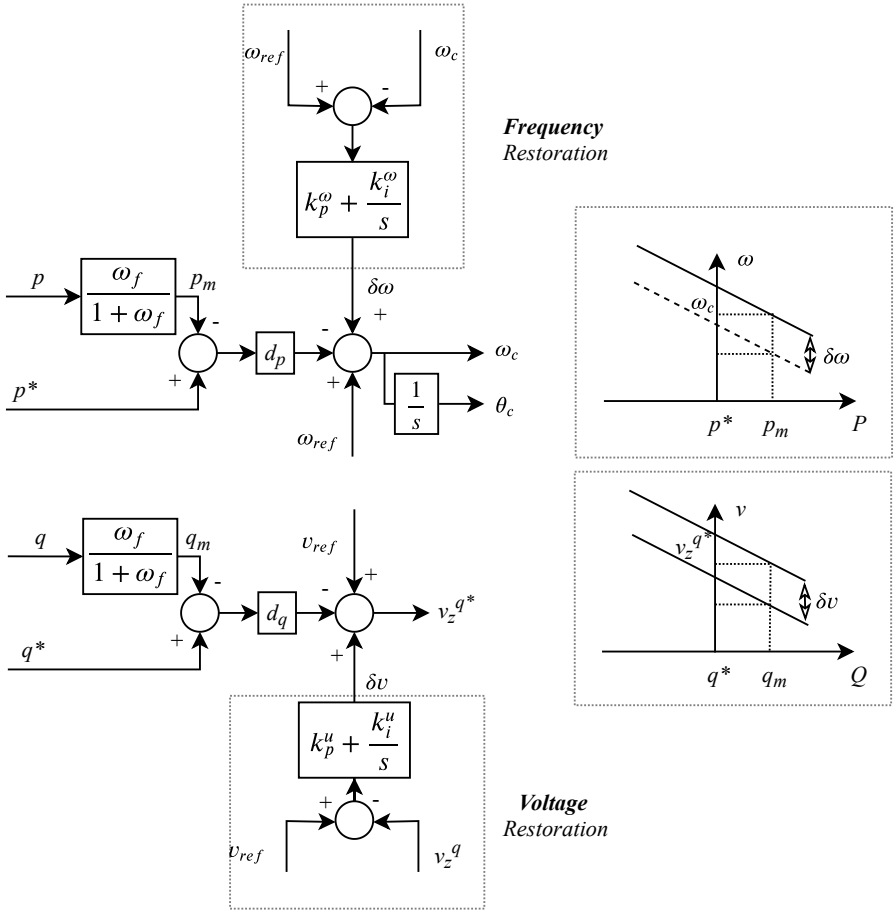

Figure 2.8: Frequency and Voltage Restoration

On the following page the control block diagram is presented in its entire form.

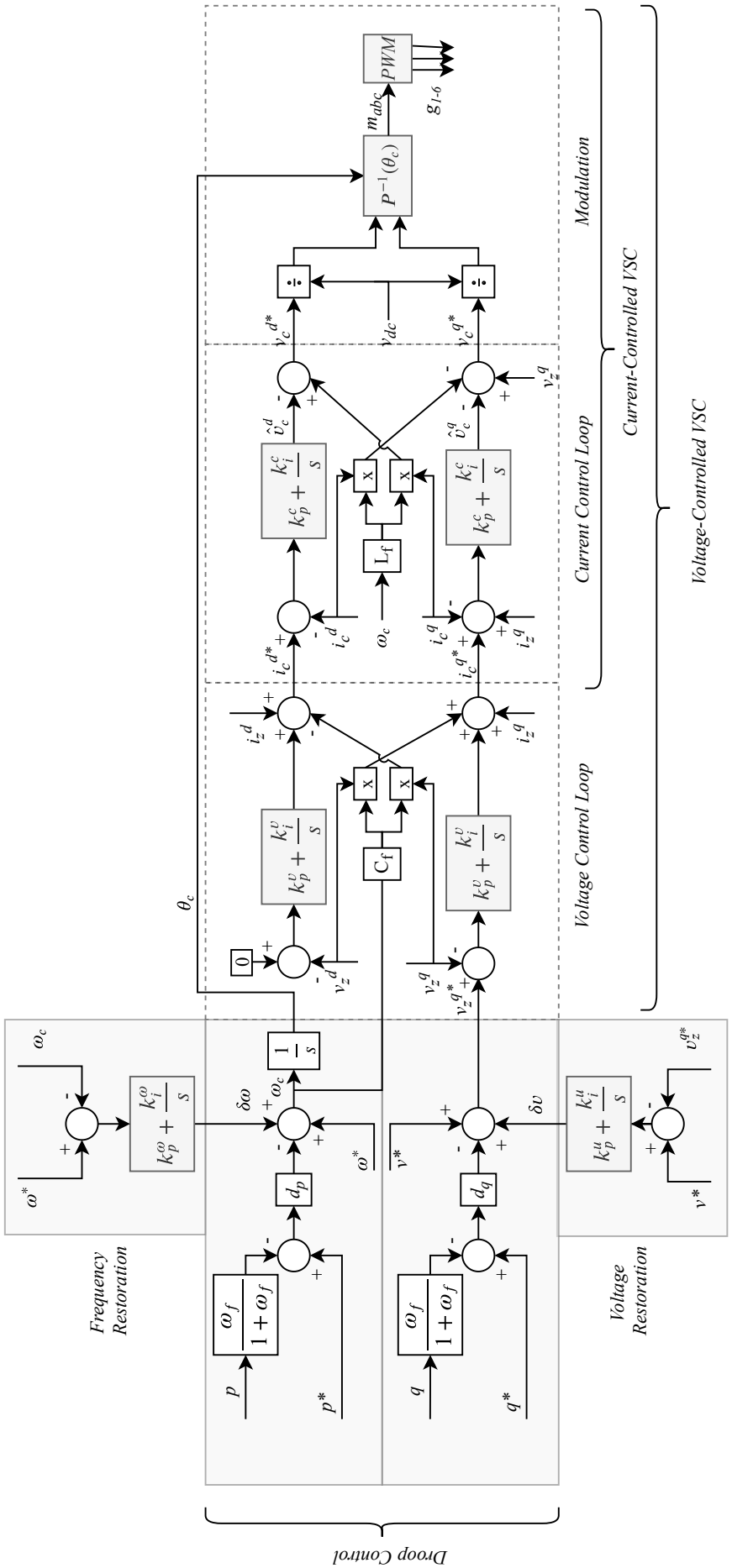

Figure 2.9: Complete VSC control schematic

2.6 Power Converter Classification

The authors of [16] differentiate VSC systems based on whether frequency is controlled or imposed, namely *Controlled-frequency VSC systems* and *Grid-imposed frequency VSC system*. In [12], converters are classified depending on their control objective, that is if the converter is *grid-forming*, *grid-feeding* or *grid-supporting*. In [11], a distinction between *grid-forming* and *grid-following* VSC system is made. In the following, these converter classifications are elaborated on.

Controlled-frequency VSC System

A frequency-controlled VSC, also referred to as a grid-forming VSC, controls the voltage amplitude and frequency at the PCC. Therefore, the active and reactive power that is exchanged between grid and converter are the by-products [16]. A typical use-case for grid-forming converters are islanded microgrids.

Grid-imposed Frequency VSC System

A grid-imposed frequency VSC system, also referred to as grid-following converter, can be further classified into the grid-feeding and the grid-supporting types. Generally, they employ a *active/reactive power controller*[16]. However, the difference lies in how the active and reactive power setpoints are generated.

For grid-feeding converters, power setpoints are rigid and either passed down from a higher management system or delivered by the DC-side of a VSC system. For grid-supporting converters, the power setpoints are variable and depend on the state of the grid at their PCC. A grid-supporting converter can be operated in *voltage-control mode* or a *current-control mode*. The former controls a voltage signal (frequency and amplitude) that will lead to the desired active and reactive power injections. The latter controls the current injected into the grid and regulates its value to achieve desired active and reactive injections. One advantage of the latter is that is allows for current protection [16].

2.7 Koh Jik Case Study

Koh Jik is a small island located on the east coast of Thailand with a population of 400 people. A microgrid has been installed in 2004, incorporating solar PV, battery energy storage and diesel generation. A metering unit has been installed in September 2018 to gather 5-minute resolution data to analyze system operation. Due to economical reasons a connection to the main grid is unfeasible.

Figure 2.10 shows the PV arrays, diesel generator and lead-acid battery bank.

Figure 2.10: Overview of centralized generation and storage assets on Koh Jik , comprising 40 kW PV, 240 kWh lead acid and 50 kW diesel

Chapter 3

Modelling

The microgrid is modelled in *Simulink* with the help of the *Simscape Power System* library. The diesel generator is not included in the scope of this thesis. The model consits of two versions:

1. **Original layout**: The load is supplied through two separate VSC systems. The VSC interfacing the battery acts as the grid-forming converter, while the VSC interfacing the PV system is operated in current-controlled, grid-feeding mode.

2. **Future layout**: The load is supplied through three separate VSC systems. In addition to the original layout, a small-scale battery unit close to the load is connected through a VSC to provide grid-supporting services.

The future layout is based on the fact that a guest-house in Koh-Jik has invested in a small-scale battery that is being charged through roof-top PV. However, the installed converter does not provide voltage support. This scenario investigates the minimum converter rating and proposes a control scheme to maintain a minimum load bus voltage of 0.95 pu during high load conditions.

3.1 Microgrid Topology

The microgrid consists of three VSCs that feed a common load (see Figure 3.1). The lines have been modelled as *RL*-elements with ($R_l = 0.642\Omega/km$) and ($L_l = 2.642 * 10^{-4} H/km$) [12]. The load is modelled as a *constant-impedance* element, which means that the power drawn depends on the load bus voltage.

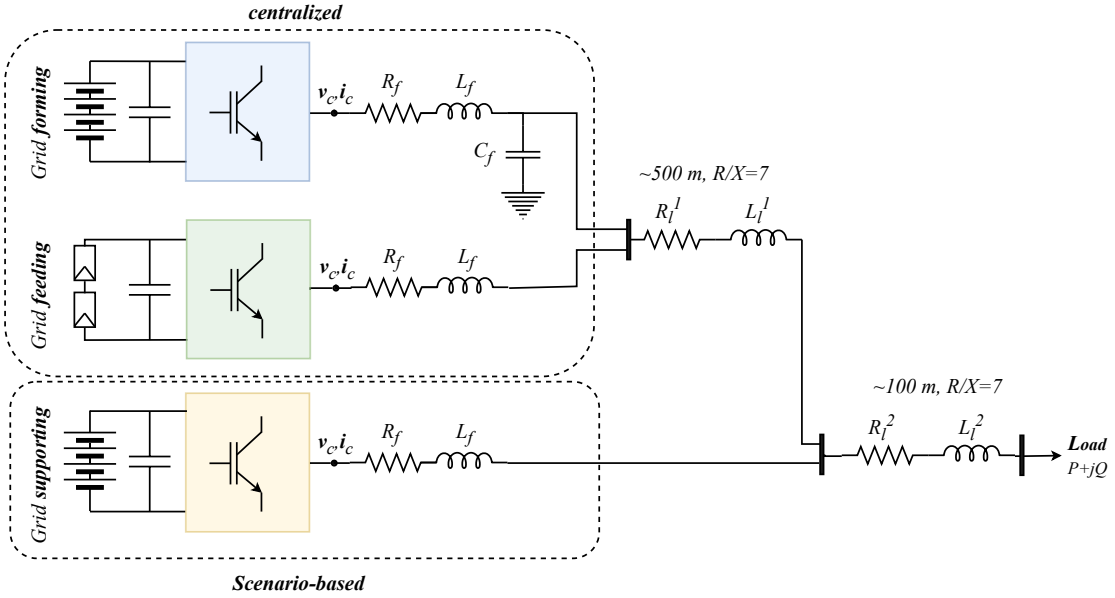

Figure 3.1: Koh Jik microgrid layout

Table 3.1 summarizes the role, rating, DC voltage source and objective of each VSC in the microgrid.

Role	**Rating S [kVA]**	**DC-source**	**Objective**
Grid-forming	50	240 kWh, centralized battery	Control frequency and amplitude of voltage at PCC
Grid-feeding	40	2x 20 kW PV arrays	Inject maximum active power
Grid-supporting	variable	Small-scale, residential battery	Adjust active and reactive power output to support voltage and frequency stability

Table 3.1: Converter overview

3.2 Converter Tuning

This section elaborates the methodology used to tune the different control loops of a VSC.

3.2.1 Current Loop Tuning

In section 2.5.2 it has been discussed that the AC-dynamics of the *RL*-filter include a coupling between q and d current components. To control each variable separately, a feed-forward was implemented which decouples the system and introduces a new control variable $\hat{v}_c^{qd}$. [16].

In their decoupled form, the system can be represented by two linear, first-order systems. Figure 3.2 shows a simplified diagram for controlling the current in qd-frame, omitting the feed-forward loop and neglecting the time delay effect of the PWM.

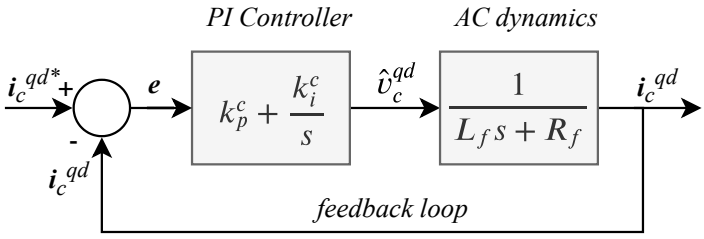

Figure 3.2: Current Control Loop

If k_p^c and k_i^c are chosen according to (3.1) the response of $i_d^{qd}(t)$ to $i_c^{qd*(t)}$ is based on a first-order transfer function, where τ_c denotes the time constant.

$$k_p^c = \frac{L_f}{\tau_c}, \qquad k_i^c = \frac{R_f}{\tau_c} \tag{3.1}$$

It is important to note that the bandwidth of the closed-loop current controller ($\omega = \frac{1}{\tau_c}$) should be at least ten times smaller than the switching frequency of the converter, expressed in *rad/s* [16].

The authors of [1] consider the delay effect of the PWM and models it as a first-order transfer function with a time constant of T_v.

$$T_v = \frac{1}{2f_{sw}} \tag{3.2}$$

Where f_{sw} denotes the switching frequency. The PI control parameters are dependent on T_v and are expressed as:

$$k_p^c = \frac{l_f}{2\omega_b T_v}, \qquad k_i^c = \frac{r_f}{2T_v} \tag{3.3}$$

Where l_f and r_f denote the per-unit values of the filter inductance and resistance and ω_b is the base angular frequency. The per-unit conversion is outlined by the authors of [2, 16].

Figure 3.3 shows the response for both *(qd)*-current components for a step-change for i^q_{ref} of 5 ampere. It can be seen that a slight coupling between *(qd)*-components is still present.

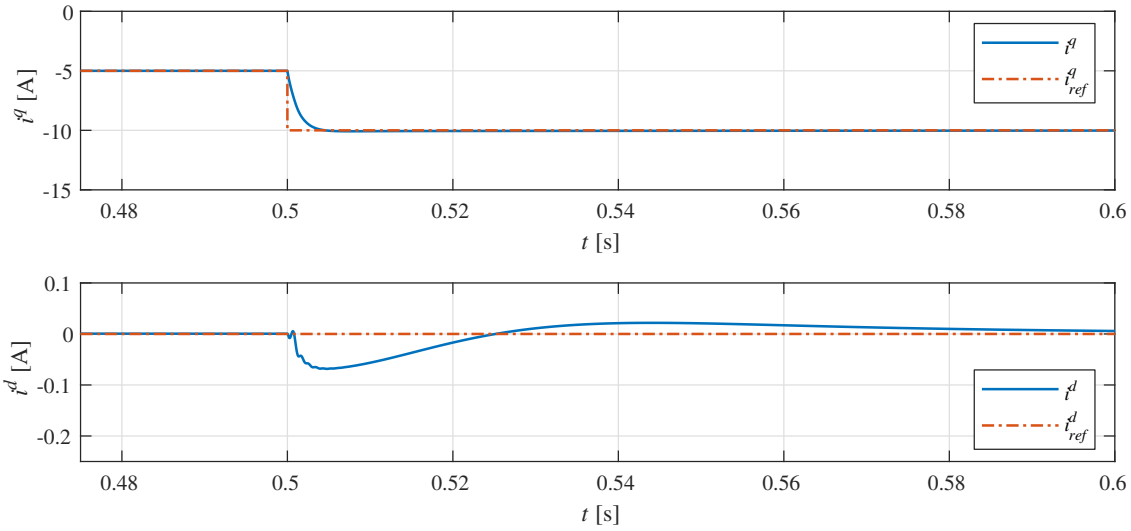

Figure 3.3: Current loop response for a step change of i^q_{ref} at $t = 0.5s$

3.2.2 Voltage Loop Tuning

This closed loop control aims at regulating the voltage (magnitude and phase) at the capacitor.

The voltage control loop computes the setpoints of the current controller, such that the correct active and reactive powers are transferred, resulting in a regulated voltage at the PCC.

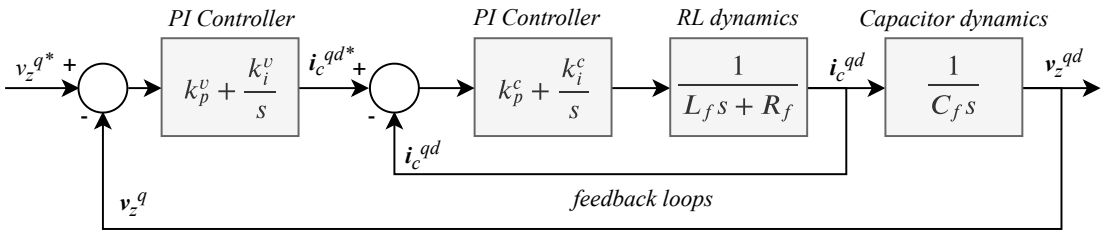

Figure 3.4: Cascaded voltage and current loop

If the time constant of the voltage control loop is chosen to be ten times slower than the current loop, its transfer function can be neglected for tuning the PI-controller [11].

The authors of [16] provide an extensive description of a tuning approach referred to as *symmetrical optimum method*. Following their approach, k_p^v and k_i^v are dependent on the time-constant of the current-loop controller (τ_c).

The authors of [1] represent the dynamics of the current loop as a first-order transfer function with a time constant of $T_{eq,c}$. The capacitor dynamics are represented by a first order transfer function with time constant T_{cap}.

$$T_{eq,c} = 2T_v, \qquad T_{cap} = \frac{c}{\omega_b} \tag{3.4}$$

Where c refers to the per-unit value of the filter capacitance C_f. The PI parameters are tuned *symmetrical optimum criterion* and are calculated as follows:

$$k_p^v = \frac{T_{cap}}{aT_{eq,c}}, \qquad k_i^v = \frac{T_{cap}}{a^3 T_{eq,c}^2}, \qquad a = 2\zeta + 1 \tag{3.5}$$

The parameter a relates k_p^v and k_i^v with the damping factor ζ of the closed-loop system response [1]. Increasing a leads to a more damped response.

Figure 3.5 shows the response for both *(qd)*-components of voltage and current for a step-change for v_{ref}^q of 0.2 p.u.

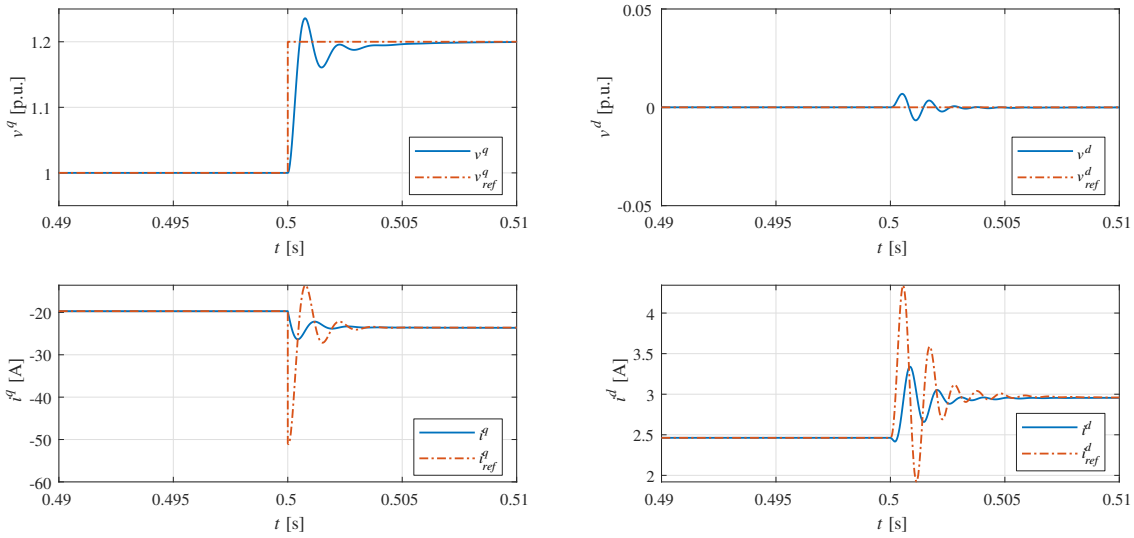

Figure 3.5: Voltage loop response for a step change of v_{ref}^q at $t = 0.5s$ by 0.2 p.u. and consequent current loop response

3.2.3 Droop Control Tuning

The authors of [10] have shown that the droop constants are critical for assessing stability. Droop constants (d_p and d_q) are usually expressed in per-unit or in percentage value. In [8], d_p and d_q of converter i are calculated as follows:

$$d_{p,i} = \frac{\omega_{max} - \omega_{min}}{P_{max,i}}, \qquad d_{q,i} = \frac{v_{z\,max}^{q} - v_{z\,min}^{q}}{2Q_{max,i}} \tag{3.6}$$

Where $\omega_{max} - \omega_{min}$ defines a frequency deviation, i.e. from 50.5 Hz to 49.5 Hz, which is acceptable for the network. If the VSC-interfaced system can also absorb power then ($d_{p,i} = \Delta\omega/2P_{max}$). If droops are represented in per-unit or percentage, the equation become:

$$d_{p,i} = r_{p,i}\frac{\omega_{ref}}{P_{max,i}}, \qquad d_{q,i} = r_{q,i}\frac{v_{z\,ref}^{q}}{Q_{max,i}} \tag{3.7}$$

Where r_p and r_q denote the percentage value.

Virtual Inertia Emulation

Virtual inertia emulation (VIE) is used in VSC to emulate the behavior of a synchronous generator. In traditional power systems, where centralized synchronous generating units are present, frequency deviations are damped due to physical inertia provided by rotating masses within the power plant.

Droop control mimics the governor response in a conventional synchronous generator. Its goal is to adjust the mechanical input power in proportion to the rotor's speed variation from nominal rpm (hence, nominal frequency). Thus, a load step will lead to *stabilized* but overall lower frequency.

However, from a stability aspect, its is beneficial to emulate the transient behavior of conventional synchronous generators during load variations. An increase in load manifests itself as a mismatch between electrical torque imposed by the AC system and mechanical torque applied by the generator shaft. The evolution of the rotor's angular frequency when subjected to a mismatch of mechanical and electromagnetic torque in described by the swing equation [5]:

$$J\frac{d\omega}{dt} = \tau_m - \tau_e - D(\omega - \omega_g) \tag{3.8}$$

Where J is the rotor inertia, τ_m the applied mechanical torque to the rotor, τ_e the electromagnetic torque imposed on the rotor by the grid and D denotes a damping coefficient that imposes a braking torque due to damper windings. ω denotes the rotating speed of the rotor and ω_g stands for the angular frequency of the grid.

Translating the original swing equation to the application of a VSC yields [10]:

$$\frac{d\omega}{dt} = \frac{1}{2H}(p^* - p) - \frac{1}{2H}K_d(\omega - \omega^*) \tag{3.9}$$

Where the first term on the RHS represents the torque mismatch and the second term imposes the damping torque. The effect of converter droop and virtual synchronous inertia are very similar. The filtering of the power measurements has

the same effect as physical inertia. The droop constant is inversely related to the damping coefficient in the swing equation. The equivalence of the terms are [5]:

$$H = \frac{1}{2\omega_f d_p}, K_d = \frac{1}{d_p} \tag{3.10}$$

Figure 3.6 shows the evolution of converter frequency during a load step for various droop constants. A higher d_p indicates a more pronounced rate of change of frequency.

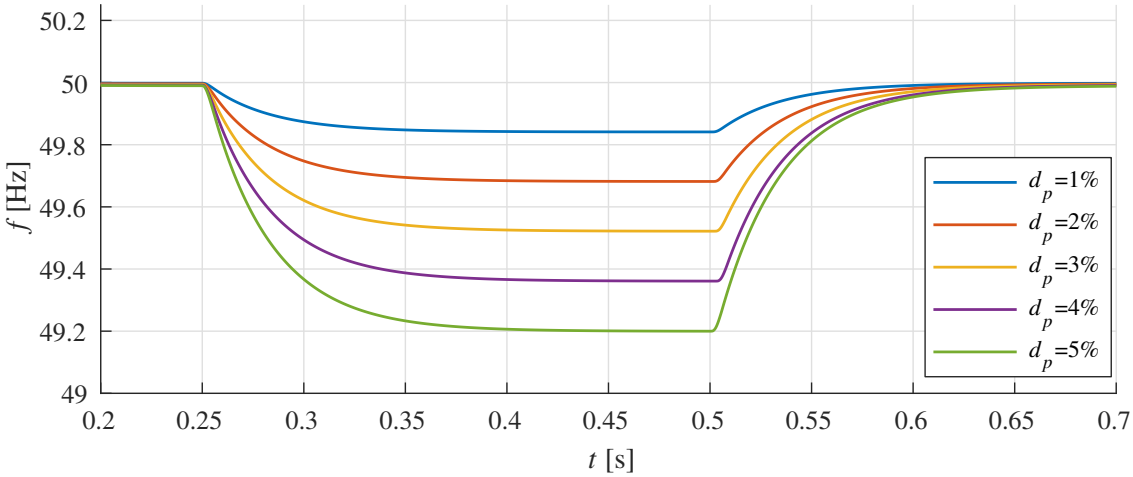

Figure 3.6: Effect of d_p variation on VSC frequency with constant corner frequency of 31.4 rad/s at load step of 15 kW

Figure 3.7 shows the effect of different LPF bandwiths. A larger corner frequency means that more high-frequency signals are passed through (i.e. higher bandwith), thus less filtering occurs. Therefore, the inertial response can be tuned by varying ω_f.

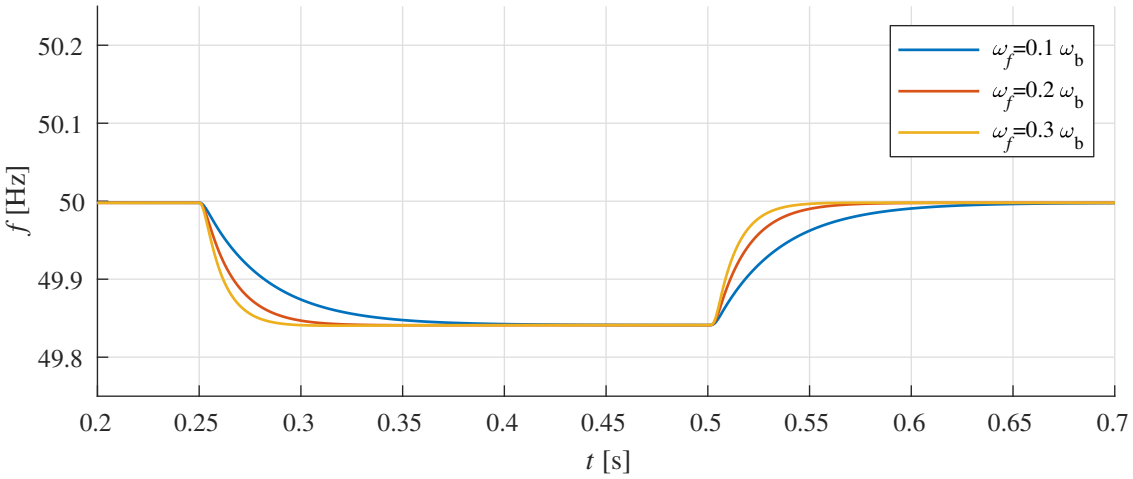

Figure 3.7: Effect of ω_f variation on VSC frequency with constant 1% d_p at load step of 15 kW

3.2.4 Droop Tuning for Current-Controlled VSC Systems

The role of the grid-supporting, current-controlled VSC is to adjust its active and reactive power to maintain a pre-defined frequency and voltage at the PCC. This can be achieved through droop control. In this application, the droop equation computes active and reactive power setpoints, which are passed directly to the power controller and subsequently to the current-control loop.

The static droop equations, rearranged for power output are:

$$p = p^* - m_p(\omega_{ref} - \lambda(s)\omega_{pll}) \tag{3.11}$$

$$q = q^* + m_q(v_z^q - v_z^{q*}) \tag{3.12}$$

Where the superscript (*) denotes a higher-level power setpoint, generally passed down from an EMS. The *P-f* and *Q-v* droop relations hold for inductive networks.

In low voltage microgrids, however, the R/X-ratio is usually around 7. In such a case, the droop relations become:

$$p = p^* - m_p\lambda(s)(v_{z,pll}^q - v_z^{q*}) \tag{3.13}$$

$$q = q^* + m_q\lambda(s)(\omega_{pll} - \omega_{ref}) \tag{3.14}$$

The droop constant m_p and m_q can be tuned according to Section 3.2.3.

3.2.5 Converter Current Limitations

The IGBTs of VSC are sized for a given maximum current. It is essential to saturate current references to avoid damaging the converter. The maximum allowable current of a converter expressed in *(qd)*-frame is:

$$i_c^{max} = \sqrt{i_c^{q2} + i_c^{d2}} \tag{3.15}$$

From its *nameplate rating* S_c, the maximum current can be deduced as:

$$i_c^{max} = \frac{S_c}{v_{pp}^{rms}\sqrt{3}}\sqrt{2} \tag{3.16}$$

Prioritizing active power injection requires to saturate i_c^d. From (3.17) it then follows:

$$i_c^{d,max} = \sqrt{i_c^{max2} - i_c^{q2}} \tag{3.17}$$

Chapter 4

Simulation and Results

This chapter discusses the simulation results for the original- and potential future layout of the microgrid. During each run an active and reactive load increase is simulated at $t = 0.25$ s, representing the peak load observed in the microgrid. At $t = 0.75$ s the load decreases to its initial value. The figures depict the development of the *(q)*-component voltage at different nodes of the microgrid as well as injected and drawn active and reactive power from different converts.

Table 4.1 summarizes the grid and converter parameters used throughout the simulation.

Grid Parameters		**Converter Parameters**	
R_l	0.642 Ω/km	R_f	31.5 $\mu\Omega$ (0.003 pu)
L_l	264 mH/km	L_f	2.4 mH (0.08 pu)
$V_{LL,rms}$	400 V	C_f	24.8 μF (0.074 pu)
f_b	50 Hz	f_s	8 kHz
Phase Locked Loop		**Current Control Loop**	
$k_{p,pll}$	0.4	$k_{p,cl}$	1.27
$k_{i,pll}$	4.69	$k_{i,cl}$	14.3 s^{-1}
Droop Control		**Voltage Control Loop**	
d_p	2 %	$k_{p,vl}$	0.59
d_q	2 %	$k_{i,vl}$	736 s^{-1}
ω_f	31.4 rad/s		
Frequency Restoration		**Voltage Restoration**	
$k_{p,f}$	200	$k_{p,v}$	200
$k_{i,f}$	4400 s^{-1}	$k_{i,v}$	4400 s^{-1}

Table 4.1: Grid and converter parameters

4.1 Original Layout

4.1.1 Single Operation of Grid-forming VSC

In this section the grid-forming converter, subscript *(gfc)*, supplies the load, subscript *(l)*, while the grid-feeding PV inverter is disconnected.

The first column of Figure 4.1 shows the *(q)*-component voltage of the converter and the load as well as active and reactive powers during the first 20 ms of the grid-forming process. During the start-up the converter has to provide an active power load of 10 kW and supply minimal capacitive reactive power due to the inductive nature of the lines. The second column shows the microgrid variables during a load increase at $t = 0.25$ s, from 10 to 25 kW and from 0.04 to 12 kVAr inductive.

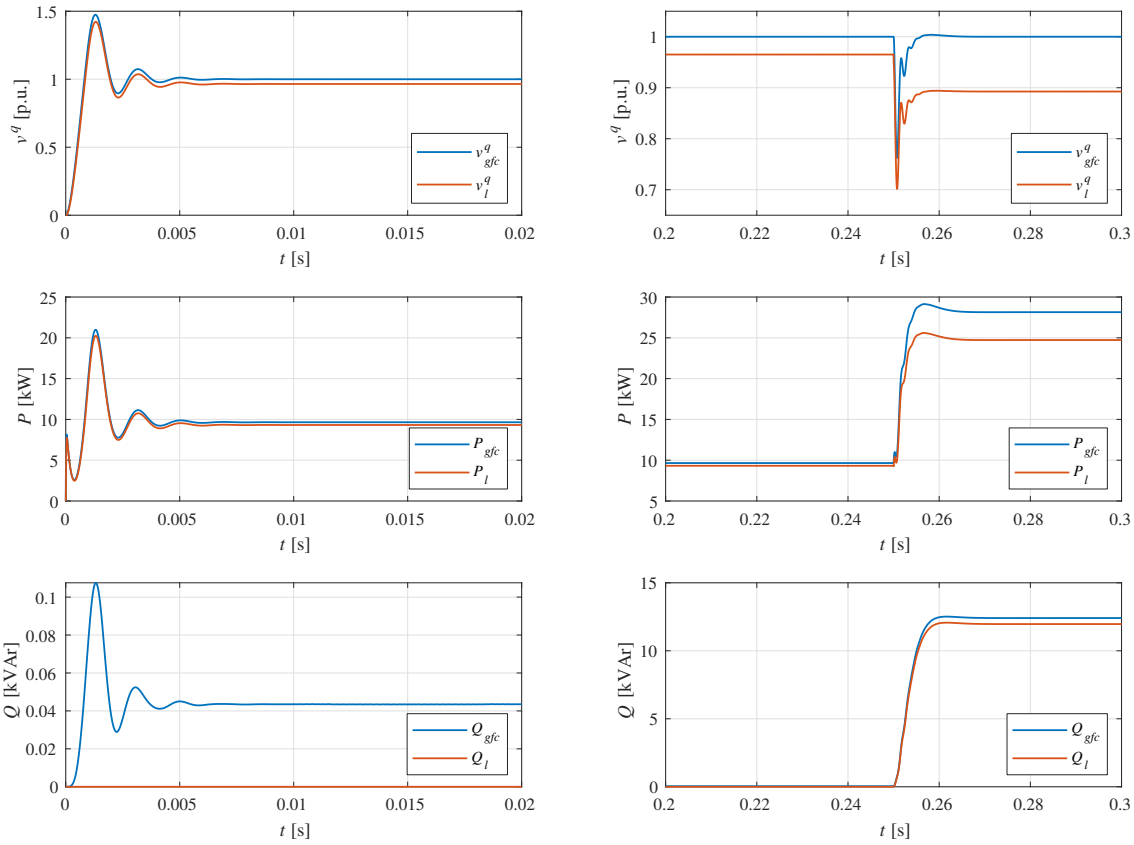

Figure 4.1: Start-up process of grid-forming VSC until $t = 0.02$ s (1^{st} column) and a load increase at $t = 0.25$ s (2^{nd} column)

It can be seen that grid-forming converter can form the grid and adequately deal with a large load deviations.

4.1.2 Grid-forming & Grid-feeding VSC Operation

In this simulation the VSC interfacing the PV array (grid-feeding unit, subscript *(pv)*) injects constant active power. It is operated in current-control mode with a PQ-controller receiving pre-defined p^* and q^* values. Normally, these are passed from the DC control system to extract the maximum power. However, the DC-dynamics are neglected in this thesis.

The first column in Figure 4.2 shows a spike in active power injection from PV at $t = 0.225$ s, from 0 to about 12 kW, leading to a voltage surge in all nodes. Since the PV power injection exceeds the load, the battery is charged until $t = 0.25$ s, when the load increases to 25 kW and 12 kVAr inductive. During the load decrease (second column) the battery returns back to charging state.

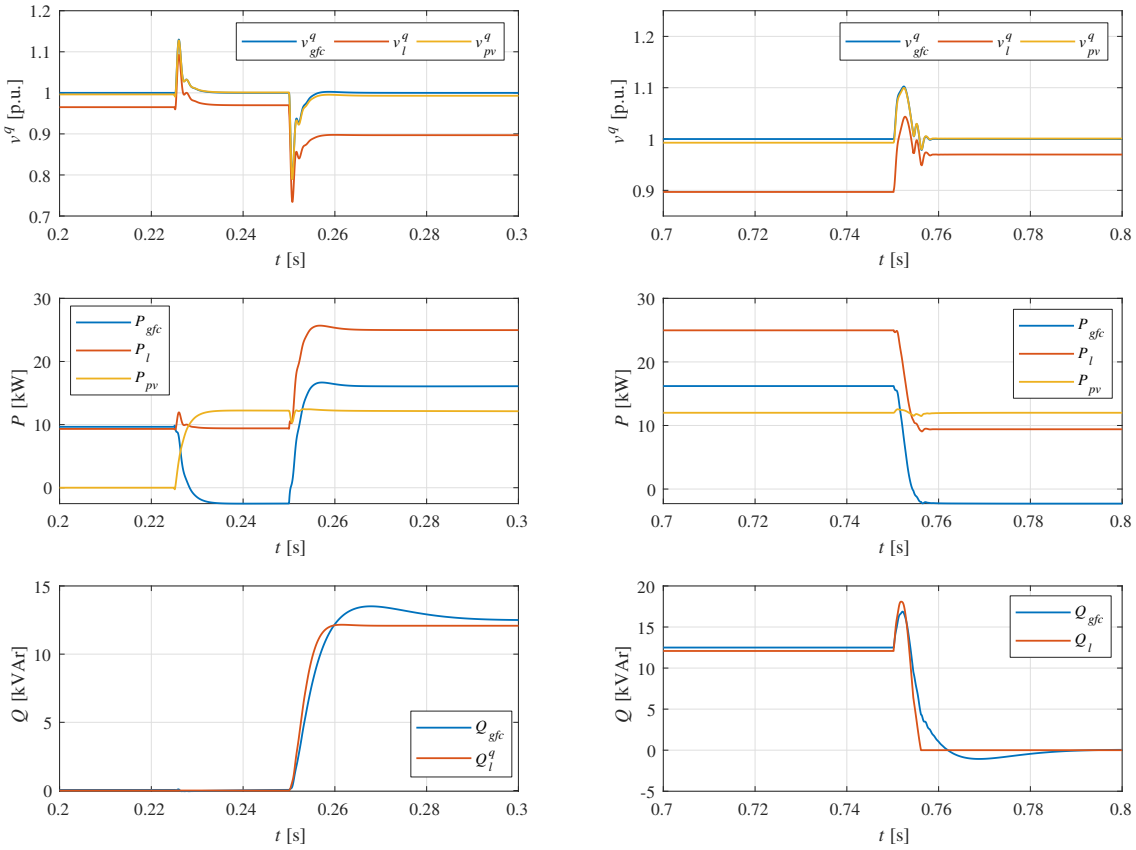

Figure 4.2: VSC interaction during a load increase at $t = 0.25$ s (1^{st} column) and a load reduction at $t = 0.75$ s (2^{nd} column)

After the load increase (1^{st} column) it can be observed that the voltage at the load bus reaches a steady-state value of 0.9 pu, violating the minimun voltage requirement of 0.95 pu.

4.2 Future Layout

In a first step, the new VSC is sized to maintain a load bus voltage of 0.95 pu during peak expected load and no contribution from PV. In a second step, control strategies are outlined and simulated, which allow the new VSC to contribute to voltage support.

4.2.1 Converter Sizing

A static AC power flow problem was solved with *MATPOWER* to evaluate the minimum kVA-rating of the converter *(G_3)*, in order to maintain a minimum voltage of 0.95 p.u. at the load bus (4) during peak load. G_2 was set to zero to model a day where no PV power is available. The load consists of 25 kW active power consumption and 12 kVAr inductive. The figure below outlines the approach:

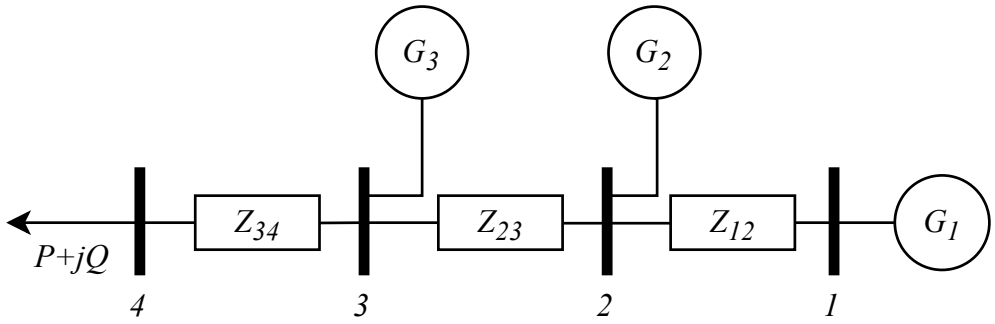

Figure 4.3: Grid Architecture for Koh Jik

Table 4.2 summarizes the parameters:

Bus Nr	**1**	**2**	**3**	**4**
Type	*Slack*	*PQ*	*PQ*	*PQ*
S_{nom}	50 kVA	0	x	na
Role	*Grid-forming*	*Grid-feeding*	*Grid-supporting*	*Load*
V_b	0.4 kV	0.4 kV	0.4 kV	0.4 kV

Table 4.2: AC Power Flow configuration

Initially, when both $G_3 = G_2 = 0$, G_1 supplies the load by itself, which leads to a load bus voltage of 0.89 pu. Through iterations it was found that the minimum rating for G_3 is 21 kVA, which yields a load bus voltage of 0.955 pu.

4.2.2 Voltage Support

In this section the dynamic interaction of a grid-forming and a grid-supporting VSC is simulated. The latter is operated in current-controlled mode with a PQ-controller, with the objective to maintain a minimum voltage of 0.95 pu at the load. For simplicity, the grid-feeding VSC is disconnected from the network during these simulations.

Figure 4.4 represents a simplified control diagram for both grid-forming (*white* background) and grid-supporting converter (*grey* background). The grid-forming VSC functions as a *power-controlled voltage source*, whereas the grid-supporting VSC functions as a *power-controlled current source*. This is highlighted in the diagram by showing the main control variable at the PCC in bold, $\boldsymbol{v_z^*}$ and $\boldsymbol{i_z^*}$, respectively. The line impedances Z_{1-3} and Z_{3-4} are colored in *blue*.

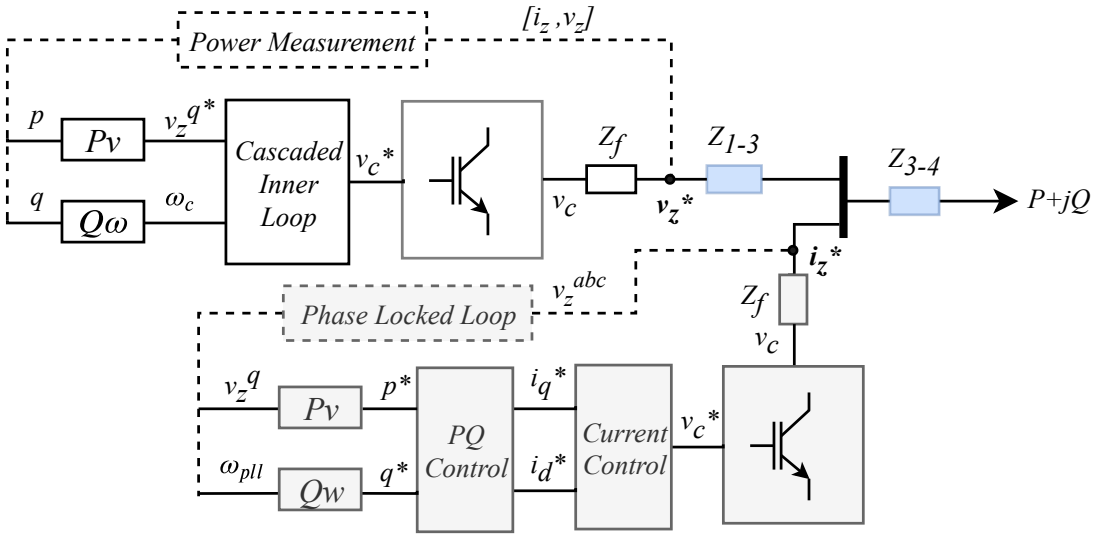

Figure 4.4: Voltage Control concept

Three different simulations are performed, one for each grid-forming VSC operating mode, defined as:

1. *Rigid* grid-forming (controlled voltage source)
2. *Droop*-based grid-forming (power-controlled voltage source)
3. *Secondary control* grid-forming (power-controlled voltage source without steady-state error)

These operating modes imply if outer control loops are employed to compute the setpoints for the cascaded inner control loop (ω_c,v_z^{q*}) of the grid-forming VSC.

Rigid Grid-forming Control

Rigid grid-forming control implies that both setpoints for the cascaded inner control loop (ω_c,v_z^{q*}) are constant values. Thus, the droop control is disabled. Therefore, the grid-forming VSC behaves as a controlled voltage source. As the load voltage is not a known quantity to the supporting converter, the PCC voltage (v_z^q) is compared with a setpoint of 0.97 pu. This setpoint is slightly larger than the minimum voltage at the load to account for the voltage drop in the downstream impedance (Z_{3-4}).

Figure 4.5 shows the adapted droop concept for active power regulation of the grid-supporting VSC. A dead band is implemented with a lower bound of 0.98 pu and an upper bound of 1 pu. This is required to avoid unnecessary participation of the VSC during low load conditions, when the voltage on the common bus exceeds 0.97 pu. In the rigid operating mode the grid-forming is represented as a controllable voltage source.

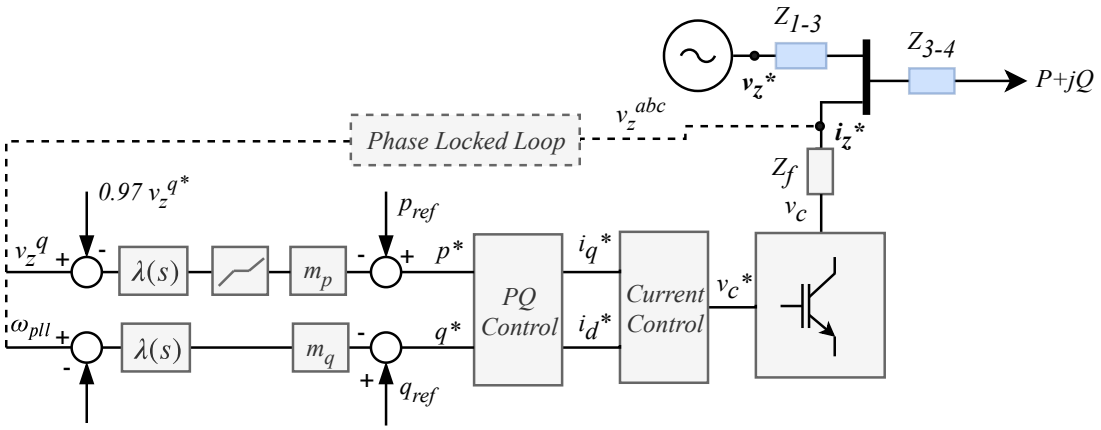

Figure 4.5: Adapted droop concept for grid-supporting VSC for active power injection

Figure 4.6 displays the interaction of the two VSC systems. Before the load step at $t = 0.25$ s, the grid-forming converter supplies the load and maintains its PCC voltage at 1 pu. At the load increase the grid-supporting VSC, subscript *(gsc)*, injects active power to reach a common bus voltage of 0.97 pu, while the forming converter downward regulates its ouput. A small reactive power injection of the grid-supporting converter is recorded due to the voltage transient and the related PLL error.

Before the load reduction at $t = 0.75$ s it can be seen that the load voltage is maintained at 0.95 pu. After the load relief the grid-supporting converter returns its active power output to zero, since its PCC voltage lies within the dead band. The voltage transient causes again a small reactive power fluctuation.

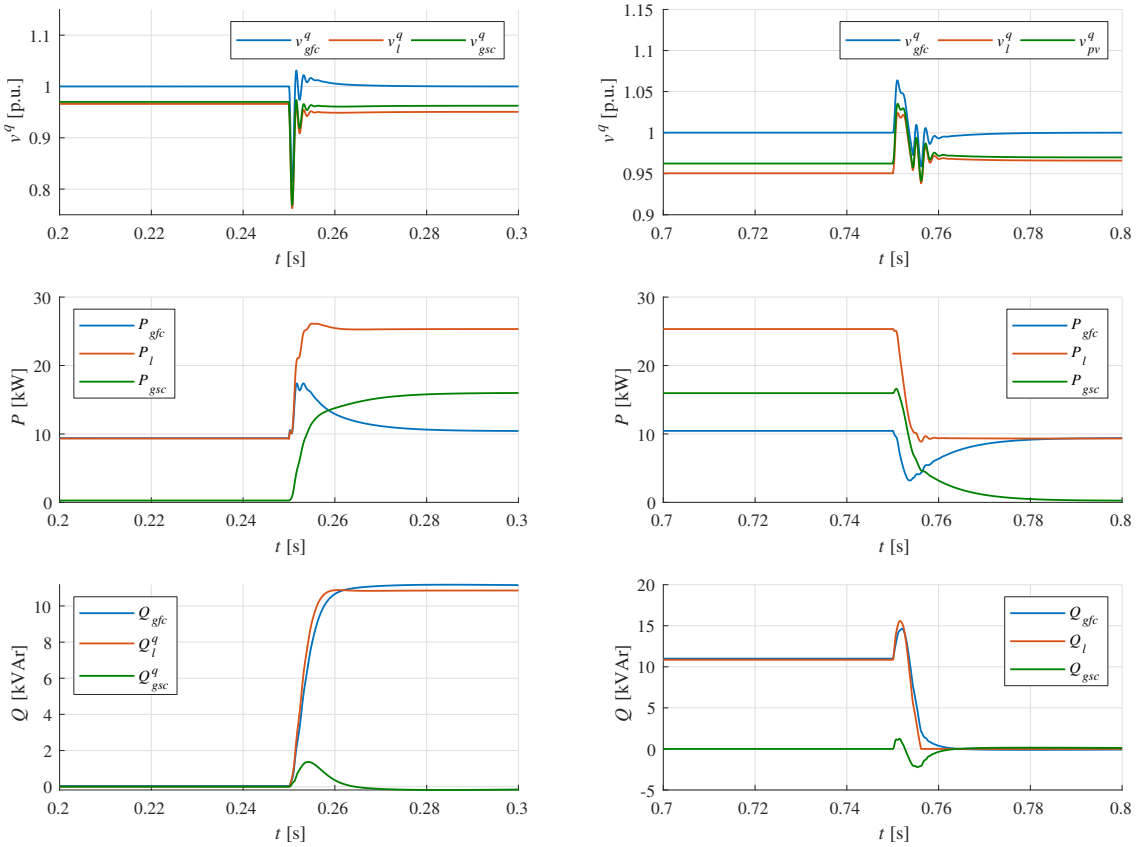

Figure 4.6: VSC interaction during a load increase at $t = 0.25$ s (1^{st} column) and a load reduction at $t = 0.75$ s (2^{nd} column)

Droop-based Grid-forming Control

In this simulation, the grid-forming VSC behaves as a power-controlled voltage source. Its setpoints for the inner cascaded loop depend on its active and reactive power output. Since the grid-supporting unit firmly controls the common bus voltage and therefore its active power injection, the frequency can be used as a signal to adjust the reactive power output of the grid-supporting converter.

Trough its droop-curve the grid-forming unit adjusts the grid frequency ω, which is being detected by the PLL of the grid-supporting converter. As no secondary control loop is implemented, a steady-state frequency error is present, which allows reactive power sharing between the VSCs.

Figure 4.7 indicates that after the load step the grid frequency is increased, which leads to reactive power sharing.

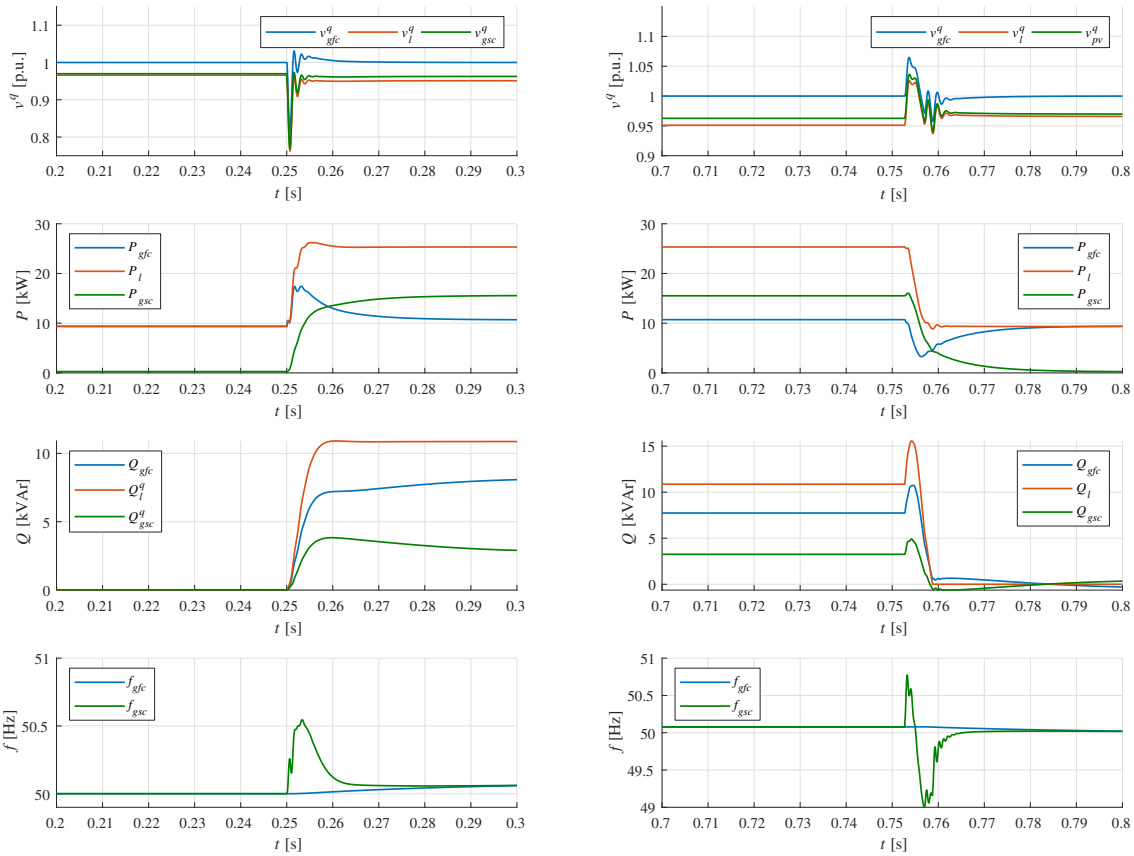

Figure 4.7: VSC interaction during a load increase at $t = 0.25$ s (1^{st} column) and a load reduction at $t = 0.75$ s (2^{nd} column)

It can be seen that the grid-supporting VSC provides constant reactive power. This is because the grid-forming VSC increases the frequency according to its droop curve. The frequency is measured by the PLL of the grid-supporting VSC and is translated into a reactive power output according to its individual droop curve. As no secondary control loop is implemented, the frequency of the voltage signal is load-dependent but can be bound in a tight range according to the grid-forming droop constant.

Droop-based Grid-forming Control with Secondary Control Loop

This simulation shows the effect of a secondary control loop driving the steady-state frequency error to zero. It is implemented at the grid-forming unit and is based on a PI-controller. Therefore, the frequency is returned to its nominal value after a load step. This causes the reactive power injection of the grid-supporting VSC to diminish over time in a regulated manner, as can be seen in Figure 4.8.

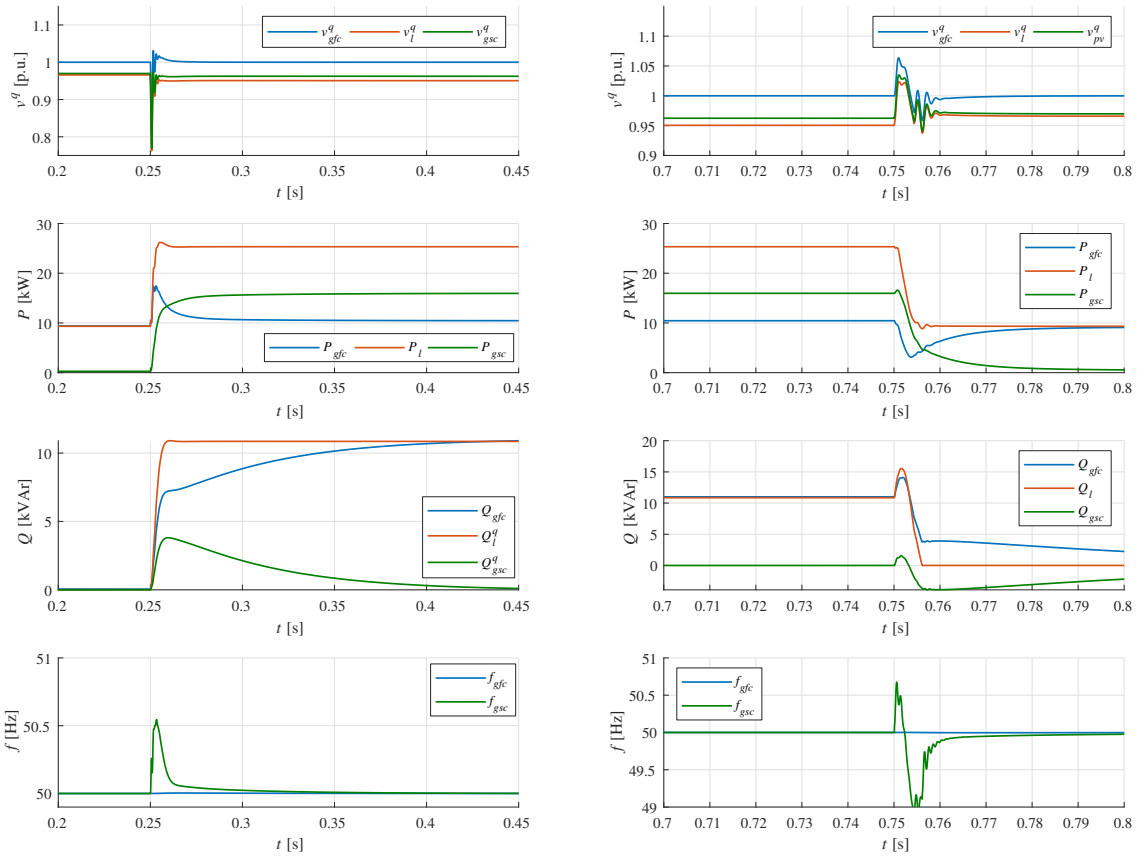

Figure 4.8: VSC interaction during a load increase at $t = 0.25$ s (1^{st} column) and a load reduction at $t = 0.75$ s (2^{nd} column)

After an initial reactive power injection of the grid-supporting VSC its output reaches zero about 20 ms after the load increase.

Chapter 5

Discussion

In this chapter the focus is set on the voltage support application through a grid-supporting VSC operated in controlled-current mode. The simulation results from Chapter 4 are investigated in greater detail, while highlighting the effect of different control parameters on stability.

5.1 Stability Considerations

The tuning parameters used in the simulations (see Table 4.1) have shown to provide well-regulated outcomes. No oscillations were introduced into the system.

The authors of [10] performed a small-signal stability analysis for converters operated in different modes. An eigenvalue analysis showed that the critical eigenvalues of the linearized state-space system was primarily influenced by the droop constants d_p and d_q. In steady-state conditions and without employing a secondary control layer, these parameters govern the load dependent frequency and voltage deviation. The corner frequency of the LPF (ω_f) was found to not have a significant influence of stability.

5.1.1 Sensitivity Analysis of d_q

The first plot in Figure 5.1 displays the microgrid frequency imposed by the grid-forming VSC for a parametrization of $d_q \in [2\%, 10\%]$ after the load increase at $t = 0.25$ s. The second plot in Figure 5.1 shows the reactive power injections of the grid-supporting converter. Note that the grid-supporting VSC relies on a PLL to measure the frequency and phase through a voltage measurements, thus its response is also dependent on its PLL performance.

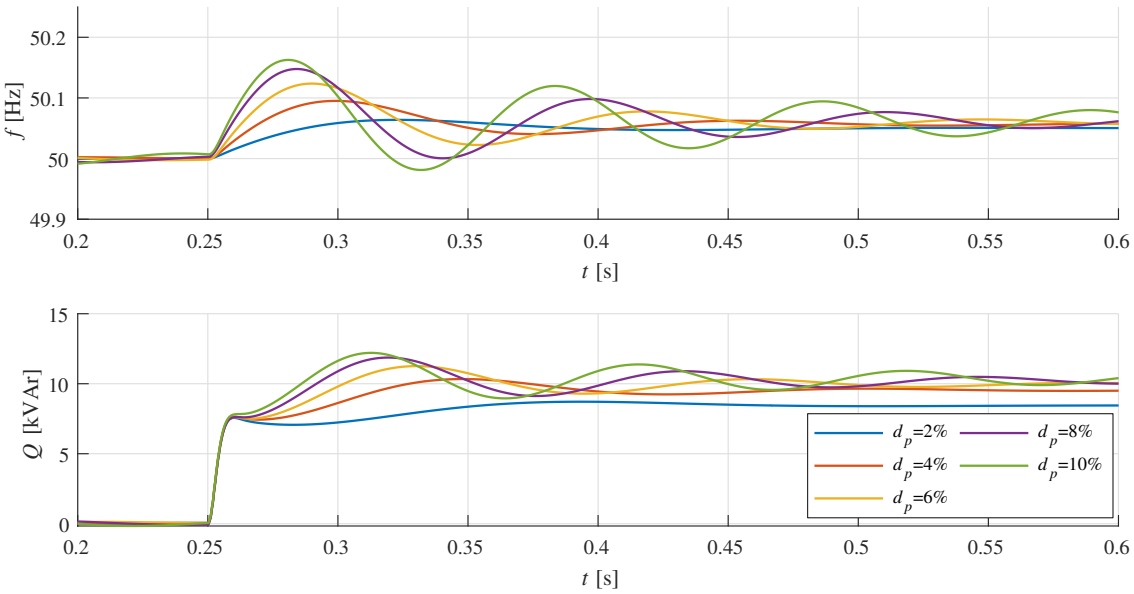

Figure 5.1: Sensitivity analysis for $d_q \in [2\%, 10\%]$

It can be seen that as d_q is increasing, frequency oscillations are amplified, resulting in oscillating reactive power injections through the grid-supporting converter. Recall that the equivalence of droop control and virtual inertia emulation in inductive networks [5]:

$$H = \frac{1}{2\omega_f d_p}, K_d = \frac{1}{d_p} \tag{5.1}$$

However, in the case of resistive LV microgrids where frequency depends on reactive power, d_p can be replaced by d_q in (5.1) and the traditional swing equation would depend on q instead of p.

Chapter 6

Conclusion and Outlook

This chapter outlines concluding remarks regarding the proposed voltage control scheme and provides an outlook for further research-work in this field.

6.1 Conclusion

In this thesis a *Simulink* model was built, representing the current and potential future layout of the islanded, low voltage microgrid on Koh Jik. The simulations showcase VSC interactions for an active and reactive load step and discuss the importance of certain control parameters on stability. The VSC control is realized in *(qd)*-frame and the cascaded current and voltage loop have been tuned according to literature [1].

Given the centralized generation layout of Koh Jik, the load bus voltage is expected to drop below 0.95 pu during high load conditions. To deal with this issue a grid-supporting VSC was successfully added to the model, located approximately 100 meters from the load center. It was found that the minimum size of the grid-supporting converter would be 21 kVA to maintain a load bus voltage of 0.95 pu during peak power consumption of the island.

The conventional droop controller of a current-controlled, grid-supporting VSC was adapted with a dead zone to supply voltage support through active power injection. The proposed control concepts rely on local measurements only. Reactive power can be shared according to droop-based frequency adjustments of the grid-forming VSC. It was found that the droop constants (d_p and d_q) of the grid-forming converter play a significant role with regards to stability. Values of d_q surpassing 4% led to amplified frequency oscillations, which in turn caused oscillating reactive power injections from the grid-supporting converter.

6.2 Outlook

In this work a three-phase balanced system was considered. Future work can investigate the VSC interaction during unbalanced loading situations and fault events. In addition, DC-dynamics can be implemented into the model.

Chapter 7

Economic and Environmental Assessment

This chapter briefly outlines the resource consumption related to this thesis and converts it to an economic and environmental cost.

7.1 Economic Assessment

The simulations were run on a *Asus Zenbook UX331U*, 8 GB RAM, Intel i5-8250/BGA laptop. The battery capacity is 3600 mAh at 11 V. During a normal workday, the laptop had to be recharged once, thus the daily electricity consumption is approximately:

$$E_{sim} \approx 3600mAh * 11V * 2 \approx 83\frac{Wh}{d} \tag{7.1}$$

The thesis was started on February 18^{th} and simulations were completed on the August 3^{rd} 2019. Not counting weekends and public holidays, this amounts to 99 days, yielding an overall electricity consumption of the laptop of 8.3 kWh. At about 24 cents per kWh this translates into an operating expense of about 2 €.

The labor expense can be approximated by assuming an hourly salary of 20 €, yielding a total cost of 13'860 €.

7.2 Environmental Assessment

The electricity consumption of the laptop can be converted into CO_2-emissions with a ratio of 0.329 $\frac{kg}{kWh}$ for the Spanish electricity mix. This yields a total output of 2,74 kg CO_2.

Bibliography

[1] Salvatore D Arco, Jon Are Suul, Olav Bjarte Fosso, and Senior Member. Automatic Tuning of Cascaded Controllers for Power Converters Using Eigenvalue Parametric Sensitivities. *IEEE Transactions on Industry Applications*, 51(2):1743–1753, 2015.

[2] C. Bajracharya, M. Marta, S. Are, and T. Undeland. Understanding of tuning techniques of converter controllers for VSC-HVDC. *Proceedings of the Nordic Workshop on Power and Industrial Electronics (NORPIE/2008)*, page 8, 2008.

[3] Claudio A Cañizares, Daniel E Olivares, Ali Mehrizi-sani, Amir H Etemadi, Student Member, Reza Iravani, Mehrdad Kazerani, Amir H Hajimiragha, Oriol Gomis-bellmunt, Maryam Saeedifard, Rodrigo Palma-behnke, Guillermo A Jiménez-estévez, and Nikos D Hatziargyriou. Trends in Microgrid Control. *Ieee Transactions on Smart Grid*, 5(4):1905–1919, 2014.

[4] Chowdhury, Crossley, and Chowdhury. *Microgrids and Active Distribution Networks*. 2009.

[5] Salvatore D'Arco and Jon Are Suul. Virtual synchronous machines - Classification of implementations and analysis of equivalence to droop controllers for microgrids. *2013 IEEE Grenoble Conference PowerTech, POWERTECH 2013*, pages 1–7, 2013.

[6] Luiz F. N. Delboni, Diogo Marujo, Pedro P. Balestrassi, and Denisson Queiroz Oliveira. *Electrical Power Systems: Evolution from Traditional Configuration to Distributed Generation and Microgrids*. 2018.

[7] Agustí Egea-Alvarez, Adrià Junyent-Ferré, and Oriol Gomis-Bellmunt. Active and Reactive Power Control of Grid Connected Distributed Generation Systems. *Modeling and Control of Sustainable Power Systems*, pages 47–81, 2012.

[8] Josep M Guerrero, Senior Member, Mukul Chandorkar, and Tzung-lin Lee. Advanced Control Architectures for Intelligent Microgrids — Part I : Decentralized and Hierarchical Control. *IEEE Transactions on Industrial Electronics*, 60(4):1254–1262, 2013.

[9] Josep M. Guerrero, Juan C. Vasquez, José Matas, Luis García De Vicuña, and Miguel Castilla. Hierarchical control of droop-controlled AC and DC microgrids - A general approach toward standardization. *IEEE Transactions on Industrial Electronics*, 58(1):158–172, 2011.

[10] Uros Markovic, Johanna Vorwerk, Petrosa Aristidou, and Gabriela Hug. Stability Analysis of Converter Control Modes in Low-Inertia Power Systems. *Proceedings - 2018 IEEE PES Innovative Smart Grid Technologies Conference Europe, ISGT-Europe 2018*, (2), 2018.

[11] T. Qoria, F. Gruson, F. Colas, X. Guillaud, M. S. Debry, and T. Prevost. Tuning of cascaded controllers for robust grid-forming voltage source converter. *20th Power Systems Computation Conference, PSCC 2018*, pages 1–7, 2018.

[12] Joan Rocabert, Alvaro Luna, Frede Blaabjerg, and Pedro Rodríguez. Control of power converters in AC microgrids. *IEEE Transactions on Power Electronics*, 27(11):4734–4749, 2012.

[13] Se-Kyo Chung. A phase tracking system for three phase utility interface inverters. *IEEE Transactions on Power Electronics*, 15(3):431–438, 2002.

[14] Inverter-based Transmission Systems. Partial Grid Forming Concept for 100% Inverter-Based Transmission Systems. 2018.

[15] T L Vandoorn, J D M De Kooning, B Meersman, and ... Review of primary control strategies for islanded microgrids with.pdf. *... and Sustainable Energy ...*, 19:613–628, 2013.

[16] Amirnaser Yazdani and Reza Iravani. *Voltage-Sourced Converters in Power Systems*. 2010.

[17] Xiaoxiao Yu, Ashwin M. Khambadkone, Huanhuan Wang, and Siew Tuck Sing Terence. Control of parallel-connected power converters for low-voltage microgrid - Part I: A hybrid control architecture. *IEEE Transactions on Power Electronics*, 25(12):2962–2970, 2010.